Journal of Physics B: Atomic, Molecular and Optical Physics

PAPER

RECEIVED
25 November 2025

REVISED
24 April 2026

ACCEPTED FOR PUBLICATION
5 May 2026

PUBLISHED
18 May 2026

Collective and individual excitations in a linear atomic chain

Hao Huang[1], **Hongcheng Ni**[1,2,*] **and Jian Wu**[1,2,3]

[1] State Key Laboratory of Precision Spectroscopy, East China Normal University, Shanghai 200241, People's Republic of China
[2] Collaborative Innovation Center of Extreme Optics, Shanxi University, Taiyuan, Shanxi 030006, People's Republic of China
[3] Chongqing Key Laboratory of Precision Optics, Chongqing Institute of East China Normal University, Chongqing 401121, People's Republic of China
[*] Author to whom any correspondence should be addressed.

E-mail: hcni@lps.ecnu.edu.cn

Abstract

Upon interaction between light and matter, particularly in solid-state materials, elementary excitations can be classified into collective and individual excitations. In this theoretical study, we investigate the interaction between a linear atomic chain and a linearly polarized laser field. Our findings reveal that both plasmon resonance, a form of collective excitation, and high harmonic generation, which arises from individual excitation, can occur simultaneously. The signals from these excitations exhibit different dependencies on the parameters of the atomic chain and the laser pulse. By adjusting factors such as pulse width, the relative intensities of these excitations can be controlled. The ability to observe and manipulate this dual excitation mode in a solid-state system lays the groundwork for further research into laser–matter interactions.

1. Introduction

When light interacts with matter, the nature of the response depends significantly on the phase of the material. In the gas phase, where atoms and molecules are isolated, the primary interaction is the excitation of individual electrons. The solid-state environment presents a more complex scenario, where dense electronic interactions give rise to intricate many-body dynamics. To simplify the description of excited states in solid-state systems, low-lying excitations, i.e., those energetically proximate to the ground state, can be effectively reduced to a collection of independent elementary excitations, known as quasiparticles, each with its own discrete energy levels. The concept of elementary excitations simplifies the complex multi-body system into a quasiparticle system that approximates an ideal gas. These excitations are broadly classified into two distinct categories: collective excitations and individual or single-particle excitations [1]. A typical example of collective excitation is the lattice wave of crystal vibration, with its corresponding quasiparticle being the phonon. Another example is the plasma oscillation, which involves the oscillation of all electrons in the solid relative to the positive ion background. The elementary excitation associated with plasma oscillation is called a plasmon, a quasiparticle representing the collective excitation of electrons. Like phonons, plasmons are classified as bosonic elementary excitations, embodying the collective behavior of electrons in response to external perturbations. Over the past several decades, the collective excitation of electrons has been extensively studied in nanostructures [2–10] and artificial atomic structures [11–13], providing valuable insights into plasmonic phenomena. [9] has reported a plasmon resonance frequency of approximately 1–2 eV in gold nanorods, lying within the characteristic energy range for metallic nanostructures.

In the context of single-particle excitations, metals provide a paradigmatic example. The Coulomb interactions between electrons induce dynamic screening, forming a charged cloud that effectively repels neighboring electrons. This screening allows the system to be modeled as a quasi-free electron gas, where the quasiparticles retain the same number density as the original electrons but acquire a modified effective mass due to many-body interactions. When subjected to a laser field, electrons can be excited from states below the Fermi level to unoccupied states above it, leaving behind holes. These excited electrons

and holes constitute single-particle excitations, or fermionic quasiparticles [14]. The subsequent motion of these electrons in the laser field and their recombination with holes leads to photon emission, which is well-described by the three-step model of high-order harmonic generation (HHG) in solids [15, 16]. The effective mean field potential experienced by electrons during HHG processes is reduced to the motion of electrons and holes on energy bands. Despite the pivotal role of multi-electron effects in solid-state HHG, the process remains reducible to a quantum-coherent superposition of multiple single-particle excitations [17–19]. Since the first experimental observation of solid-state HHG by Ghimire *et al* [20] in 2011, the phenomenon has been extensively studied across diverse condensed-phase systems. HHG has now been reported in semiconductors [21, 22], nanostructures [23, 24], topological insulators [25, 26], and other solid-state materials. Concurrently, a variety of theoretical approaches have been developed to analyze HHG in solids, including the single-particle time-dependent Schrödinger equation [27], semiconductor Bloch equations [28–30], density matrix methods [31], and time-dependent density-functional theory (TDDFT) [32–35]. These methods provide complementary insights into the interplay of band structure, many-body effects, and ultrafast laser-driven dynamics. Among these, TDDFT offers a distinct advantage by enabling a unified, first-principles and scalable treatment of both individual and collective excitations, capturing electron correlations to a significant extent, which is challenging for many other methods [36]. Furthermore, its real-space formulation naturally accommodates finite and confined geometries, making it ideally suited for studying size-dependent plasmonic and nonlinear optical responses in nanoscale systems.

Recent years have witnessed significant advances in the study on elementary excitations in solids, particularly plasmon resonances and HHG, which have greatly advanced related fields. Examples include: generation of ultrafast coherent short-wavelength light sources via solid-state HHG [37, 38] and its application in probing electronic states in materials [16]; development of precise molecular identification and viral imaging techniques through plasmonic spectroscopy [39]; efficient modulation and enhancement of thermoplasmonic effects via resonance mechanisms [40, 41]; and application of multi-wavelength lasers as high-quality pumping sources for these processes [42]. These advances collectively underscore the applications of HHG and plasmonics in coherent light sources, precision imaging, and thermoplasmonic, highlighting the significance of investigating their underlying physical mechanisms.

The linear atomic chain is a foundational model in solid-state physics, widely employed in theoretical studies of plasmon resonance [43–46] and HHG in solids [32, 34, 47–51]. The dipole response of this system serves as a key observable, capturing signatures of both plasmonic excitations and harmonic emission. While previous works, such as Bauer and Hansen [34], have observed the non-HHG signals (which we identify as plasmon resonance) that originate from the polarization of the metallic atomic chains in the laser field, a detailed comparative analysis of these phenomena, which root in distinct excitation mechanisms, has yet to be conducted.

In this work, we present a unified analysis of plasmon resonance and HHG signals within the framework of laser-driven dipole response of a linear atomic chain. This approach directly probes the coexistence of collective and single-particle excitation mechanisms within the system. We systematically analyze the frequencies of signals associated with both excitation mechanisms and the spatiotemporal characteristics of plasmon resonance. Through systematic variation of atom number and lattice constant, we characterize the dependence of the plasmon resonance frequency on the atomic chain parameters. Specifically, we demonstrate that changing the laser wavelength alters only the HHG frequency, while adjusting the pulse width selectively enhances one excitation mode over the other. Furthermore, resonant enhancement occurs when the laser frequency matches the plasmon frequency, leading to significant amplification of the overall signal intensity. With these observations, we establish a framework for disentangling and manipulating collective and single-particle excitations, advancing the fundamental understanding and potential applications in light–matter interaction.

The article is organized as follows. In section 2, we present the theoretical framework, including the linear atomic chain model and numerical methods. In section 3, we demonstrate that collective and individual excitations exist simultaneously in the linear atomic chain. In section 4, we present a systematic investigation of how atomic chain parameters and laser field characteristics influence the system's dipole response, with particular emphasis on the interplay between collective and single-particle excitation modes. Conclusions are given in section 5. Atomic units are used throughout unless stated otherwise.

2. Theoretical framework

We model a one-dimensional linear atomic chain consisting of N singly charged ions fixed at positions $x_i = [i-(N+1)/2]a$, where a is the lattice constant, as illustrated in figure 1(a). The electron-ion interaction is described by a soft-core Coulomb potential:

$$v_{\text{ion}}(x) = -\sum_{i=1}^{N} \frac{1}{\sqrt{(x-x_i)^2+1}}. \tag{1}$$

To account for electron–electron interactions self-consistently, we employ TDDFT within the local spin-density approximation (LSDA) [34]. This choice is well-suited for our one-dimensional metallic atomic chain, whose charge density distribution remains largely uniform along the chain and thus closely resembles the homogeneous electron gas for which LSDA is formally exact. As demonstrated in previous work on finite atomic chains [43], the TDDFT framework reliably captures the transition from single-particle (atom-like) excitations to collective plasmon resonances once the system size exceeds the threshold (N>3) and exhibits characteristic solid-state behavior. While we acknowledge inherent limitations, including non-uniformity at the chain ends, transient density fluctuations under laser driving, and the lack of non-local dynamical correlations which can be enhanced in low-dimensional systems, LSDA nonetheless provides a robust, computationally efficient foundation that captures the essential physics of the collective and single-particle excitations examined here. We note that the qualitative conclusions of our work are expected to remain robust under higher-precision functionals (e.g. GGA, meta-GGA), as they reflect fundamental physical principles of the system, which may quantitatively refine spectral intensities and peak widths by better accounting for non-local correlation effects. Furthermore, for uniform electron-gas-like systems, LSDA typically yields more accurate plasmon energies than the random-phase approximation, which omits exchange-correlation effects [43].

In TDDFT methods, system dynamics are governed by the time-dependent Kohn–Sham (KS) equations for spin orbitals $\psi_{\sigma,i}(x,t)$:

$$\mathrm{i}\partial_t \psi_{\sigma,i}(x,t) = \left[-\frac{1}{2}\frac{\partial^2}{\partial x^2} + v_{\text{KS}}[n_\sigma](x,t)\right]\psi_{\sigma,i}(x,t), \tag{2}$$

where the KS potential v_{KS} comprises four components:

$$v_{\text{KS}}[n_\sigma](x,t) = v_{\text{ion}}(x) + u[n](x,t) + v_{\text{xc}}[n_\sigma](x,t) + x\cdot F(t), \tag{3}$$

where $u[n](x,t) = \int n(x',t)[(x-x')^2+1]^{-1/2}\mathrm{d}x'$ is the Hartree potential, $v_{\text{xc}}[n_\sigma](x,t) \approx -[(6/\pi)n_\sigma(x,t)]^{1/3}$ is the exchange-correlation (xc) potential in the LSDA, $n_\sigma(x,t) = \sum_{i=1}^{N_\sigma}|\psi_{\sigma,i}(x,t)|^2$ is the spin density for spin $\sigma = \uparrow,\downarrow$, $n(x,t) = \sum_\sigma n_\sigma(x,t)$ is the total single-particle density, and $F(t)$ represents the laser electric field linearly polarized along the chain.

We propagate the KS orbitals using a Numerov-improved Crank–Nicolson method [52], which provides fourth-order accuracy in spatial discretization without requiring reduced grid spacing or significant additional computational cost in comparison to the Crank–Nicolson method. To accurately model plasmon resonances in finite atomic chains, open boundary conditions are employed rather than periodic ones. It is noteworthy that in the subsequent calculations, the plasmon resonance frequencies exhibit strong dependence on open boundary conditions and the edge localization of the atomic chain, as they encode the finite nature of the system. Periodic boundary conditions that model an infinite chain would fail to capture these effects, leading to unphysical results for finite chains. Furthermore, a sufficiently extended spatial grid with absorbing boundary layers is implemented to effectively suppress unphysical reflections from the grid edges. In the absence of the laser field, $F(t) \equiv 0$, equation (2) becomes stationary reduces to the time-independent KS equation:

$$\epsilon_{\sigma,i}\psi_{\sigma,i}(x) = \left[-\frac{1}{2}\frac{\partial^2}{\partial x^2} + v_{\text{KS}}[n_\sigma](x)\right]\psi_{\sigma,i}(x), \tag{4}$$

where $\epsilon_{\sigma,i}$ is the KS orbital energy. The stationary KS ground-state orbitals and energies are obtained via imaginary-time propagation with Gram–Schmidt orthogonalization.

Figure 1(b) displays the electronic band structure of the linear atomic chain with lattice constant $a = 2$ a.u. and $N = 100$ ions/electrons in a spin-neutral configuration $N_\uparrow = N_\downarrow = N/2$. The periodic arrangement consisting of equally spaced atoms leads to a half-filled metallic band structure, where the KS orbitals below the dashed line (Fermi level) represent occupied states.

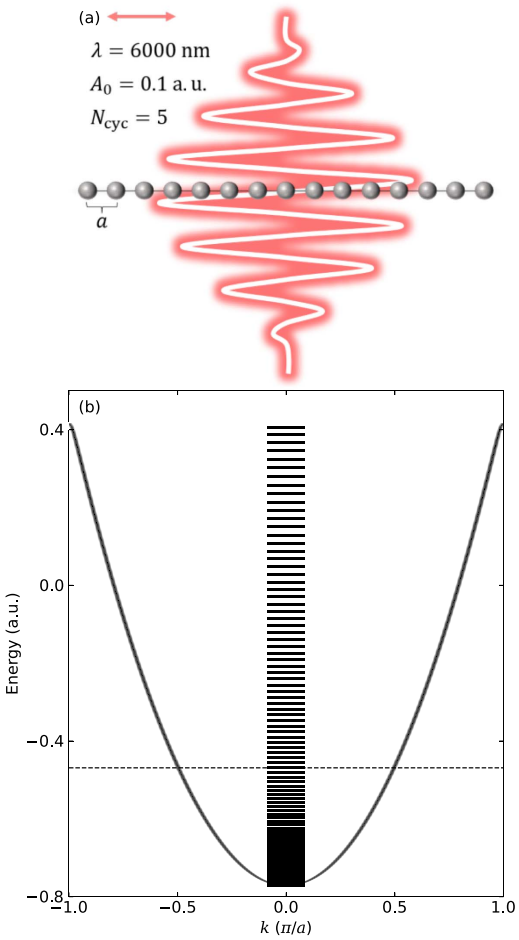

Figure 1. (a) Schematic diagram of the interaction between a one-dimensional linear atomic chain and a linear polarized laser. The arrow indicates that the laser polarization direction is parallel to the atomic chain. (b) Electronic band structure of the linear atomic chain system ($N = 100$ atoms, lattice constant $a = 2$ a.u.). The short horizontal lines indicate Kohn–Sham orbital energies $\epsilon_{\sigma,i}$, with occupied states shown below the dashed line (Fermi level).

To explore the interaction between the laser field and the linear atomic chain, we apply a linearly polarized laser pulse along the atomic chain. Within the dipole approximation, the pulse is described by the vector potential:

$$A(t) = A_0 \sin^2\left(\frac{\omega t}{2N_{\rm cyc}}\right)\sin(\omega t), \tag{5}$$

where the total number of optical cycles $N_{\rm cyc} = 5$, laser frequency $\omega = 0.0076$ a.u. corresponding to a wavelength of $\lambda = 6\,\mu$m, and the vector potential amplitude $A_0 = 0.1$ a.u. corresponding to a laser intensity of approximately $2 \times 10^{10}\,{\rm W\,cm^{-2}}$ and a field strength of approximately $3.88 \times 10^6\,{\rm V\,cm^{-1}}$. Such laser parameters are experimentally feasible using state-of-the-art mid-infrared sources, such as optical parametric amplifiers, synchrotrons, or free-electron lasers, and correspond to non-destructive excitation conditions commonly employed in strong-field solid-state studies. Under the length gauge, the KS potential becomes time-dependent due to its dependence on the electron density. The time-dependent KS potential is updated self-consistently at each time step to capture the full electron dynamics. We calculate the dipole response by Fourier transforming the dipole moment $D(\omega) \propto |\mathcal{F}[X(t)]|^2$, where

$$X(t) = \sum_{i,\sigma}\int x|\psi_{\sigma,i}(x,t)|^2 {\rm d}x. \tag{6}$$

3. Collective and individual excitations

Figure 2(a) presents the dipole response spectra for the linear atomic chain with various length N at a fixed lattice constant $a = 2$ a.u. The spectra reveal two distinct excitation modes: (1) HHG peaks at odd multiples of the laser frequency, and (2) plasmon resonances whose frequencies depend strongly on chain length.

The fact that HHG signals emerge at frequencies of the fundamental laser and its third harmonic, which arises from single-particle excitations, is independent of the chain length. As expected for a centrosymmetric system under linear polarization, even-order harmonics are symmetry-forbidden, leaving only odd harmonics observable. At higher orders, the HHG signal becomes overwhelmed by intense plasmon resonances, or, collective electron oscillations, that scale with system size.

The colored markers in figure 2(a) identify the first four plasmon modes ($n = 1, 2, 3, 4$). These exhibit two characteristic size-dependent behaviors: (1) a redshift in resonance frequency with increasing N, and (2) enhanced intensity for longer chains. These trends agree with prior studies of the longitudinal plasmon resonance of linear sodium chains [44, 45], where the redshift reflects reduced dipole excitation energy gaps in longer chains, while the intensity enhancement stems from greater electron participation in the collective oscillation.

The observed redshift with increasing atom number can be quantitatively reproduced through classical electrodynamics calculations of Mie frequencies (for $n = 1$ only) using a simple ellipsoidal model, as shown in figure 3. In our calculations, the frequencies of the ellipsoid are determined by the poles of its polarizability [45]

$$\alpha(\omega) = \frac{4\pi xyz}{3} \frac{\epsilon(\omega) - \epsilon_m}{\epsilon_m + n_i[\epsilon(\omega) - \epsilon_m]}. \tag{7}$$

Here, we use $\epsilon_m = 1$ for the atomic chain and a Drude dielectric function $\epsilon(\omega) = 1 - \omega_p^2/\omega^2$ [53]. The form factor n_i $(i = x, y, z)$ is calculated by [45]

$$n_i = \frac{xyz}{2} \int_0^\infty \frac{\mathrm{d}s}{(s + i^2)\sqrt{(s + x^2)(s + y^2)(s + z^2)}}, \tag{8}$$

where x, y, z are the half axes of the ellipsoid. The geometry of the atomic chain is given by $y = z = R$ and $x = R + (N - 1)a/2$. With $R = 2$ a.u. and $\omega_p = 0.8489$ eV, we find a perfect fitting to the first-order plasmon resonance frequencies calculated by TDDFT. This agreement between our quantum-mechanical simulations and classical continuum modeling demonstrates that the plasmon resonance fundamentally arises from macroscopic polarization effects, despite its atomic-scale origin.

In order to analyze the plasmon resonance characteristics, we demonstrate in figure 2(b) the spatial profiles of the induced electron density at the first four resonance frequencies of the atomic chain with $N = 100$. These spatial profiles $n(x, \omega_{n=1,2,3,4})$ are obtained from Fourier transform of the time-dependent density resonance $n(x, \omega) = \mathcal{F}[n(x, t)]$ at the corresponding frequencies. The spatial profiles reveal key features of quantized plasmon modes: (1) each mode shows characteristic asymmetric density distributions, with electron accumulation at one chain end and depletion at the other, which is a clear signature of dipole-active plasmon excitations [44], (2) the number of density oscillation nodes precisely matches the plasmon order n, demonstrating the standing-wave quantization of one-dimensional plasmons, and (3) superimposed on these global oscillations are rapid density variations localized at atomic sites, arising from intra-atomic potential confinement, which creates a fascinating interplay between delocalized quantization across the chain and localized electron confinement at atomic sites. The persistence of these competing length scales suggests an important research direction regarding how universal this competition in other nanostructures is. Previous work [45] hints this may be a general phenomenon in atomic-scale plasmonic systems.

To further demonstrate the macroscopic polarization characteristic of plasma resonance, we have mapped the time-dependent density fluctuations $n(x, t) - n(x, 0)$ of the linear atomic chain with $N = 100$, $a = 2$ under laser excitation, as displayed in figure 4. The blue curve in figure 4 is the electric field of the laser pulse. Remarkably, the charge density of the system undergoes electric-field-induced polarization, demonstrating the macroscopic polarization effect of plasma resonance. Interestingly, the polarization is virtually synchronized to the electric field, displaying a vanishing 'polarization time delay'. This is arguably due to the fact that intrinsic timescale of the collective electron motion is faster than the external field, and thus is capable of following the change in the laser field.

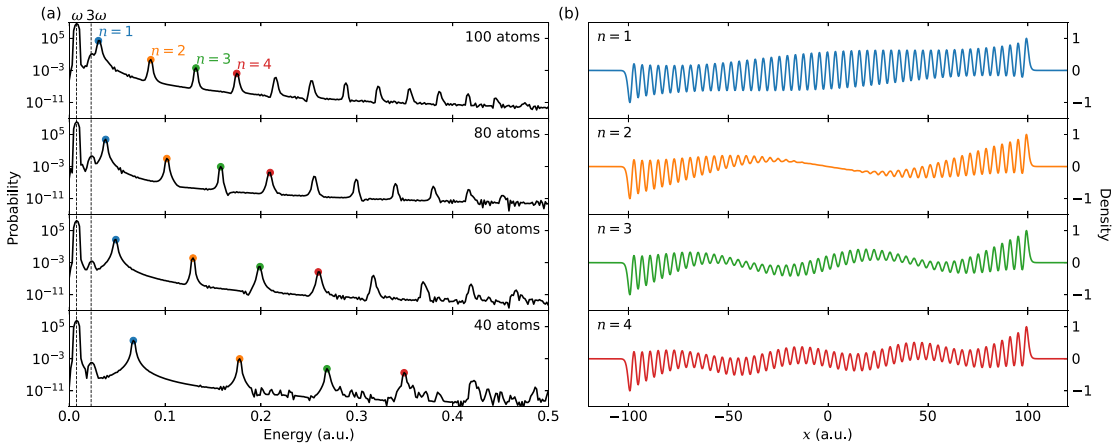

Figure 2. (a) Dipole response spectra for the linear atomic chain with various number of atoms N and fixed lattice constant $a = 2$ a.u. Colored markers represent the first four plasmon resonance frequencies ($n = 1, 2, 3, 4$). (b) Spatial profiles of the induced electron density at each plasmon resonance for $N = 100$ and $a = 2$ a.u., normalized to highlight the distinct charge oscillation patterns corresponding to different plasmonic modes.

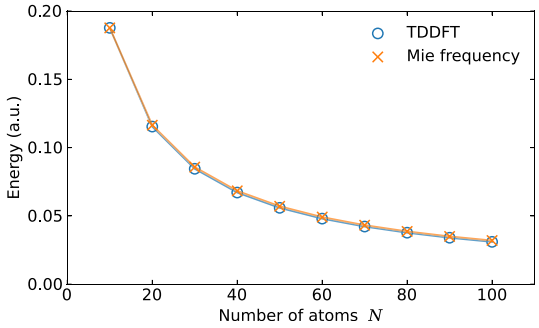

Figure 3. A comparison of the first-order ($n = 1$) plasmon resonance frequencies calculated by TDDFT with the Mie frequencies of the ellipsoidal model for different number of atoms.

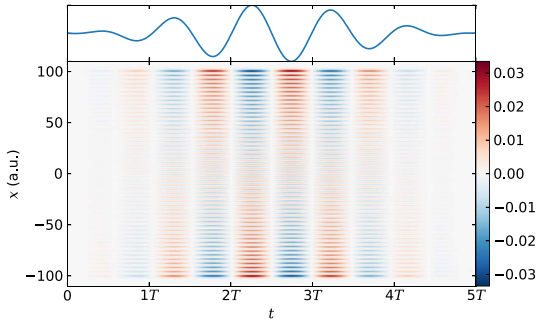

Figure 4. The time-dependent density fluctuations $n(x, t) - n(x, 0)$ of the system. The blue curve above denotes the electric field of the laser pulse.

4. Tunable control of dipole response in atomic chains

Figures 5(a) and (b) systematically characterize how the first four plasmon modes ($n = 1, 2, 3, 4$) depend on (a) atom number N (with fixed $a = 2$ a.u.) and (b) lattice constant a (with fixed $N = 100$). While high harmonic frequencies (not shown) are determined solely by the driving laser field, the plasmon resonances exhibit two key scaling behaviors: (1) All plasmon modes redshift with increasing chain length $L = N{\cdot}a$, whether through larger N or a. This follows the expected $1/L$ scaling for confined plasmonic systems. (2) The frequency shifts reveal distinct dependences on N versus a variations, indicating that plasmon energies are not simply determined by total length L alone. Rather, they reflect subtle

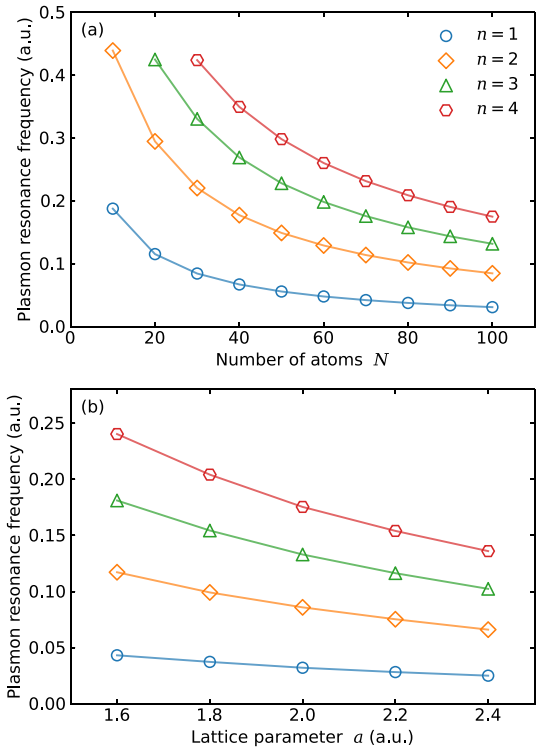

Figure 5. Scaling of the first four plasmon resonance modes ($n = 1, 2, 3, 4$) with system parameters: (a) dependence on atom number N at fixed lattice constant $a = 2$ a.u., showing characteristic redshift with increasing system size. (b) Dependence on lattice constant a for fixed $N = 100$ atoms. Both panels demonstrate characteristic redshifts.

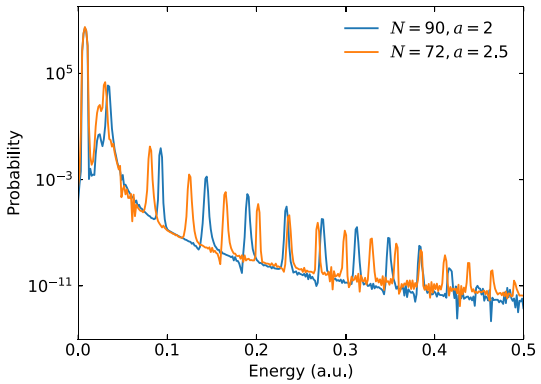

Figure 6. Dipole response spectra for the linear atomic chain with different parameter combinations of ($N = 90, a = 2$ a.u.) versus ($N = 72, a = 2.5$ a.u.), maintaining identical chain length $L = N{\cdot}a$.

differences in electron density distributions arising from discrete (N-changing) versus continuous (a-changing) length modifications. These observations demonstrate that while chain elongation generally reduces plasmon frequencies, the microscopic arrangement of atoms plays a crucial role in determining the exact scaling behavior. This has important implications for designing plasmonic systems where both the number of atoms and their spacing can be independently controlled.

To isolate the individual roles of atom number N and lattice constant a, figure 6 compares dipole responses for two configurations with identical chain length $L = N{\cdot}a$: (1) ($N = 90, a = 2$ a.u.) and (2) ($N = 72, a = 2.5$ a.u.). It is easy to find that all plasmon resonances are systematically redshifted for the ($N = 72, a = 2.5$ a.u.) case compared to the ($N = 90, a = 2$ a.u.) configuration, and the frequency shift increases progressively with plasmon order n. This demonstrates that plasmon resonances are sensitive not just to macroscopic length scales, but to the microscopic details of electronic confinement, where variations in the atom number and the lattice constant exert distinct influences on the modulation of the energy gaps. As the number of atoms N increases, the band structure depicted in figure 1 remains invariant. Nevertheless, the count of energy levels, denoted by the short horizontal lines in figure 1,

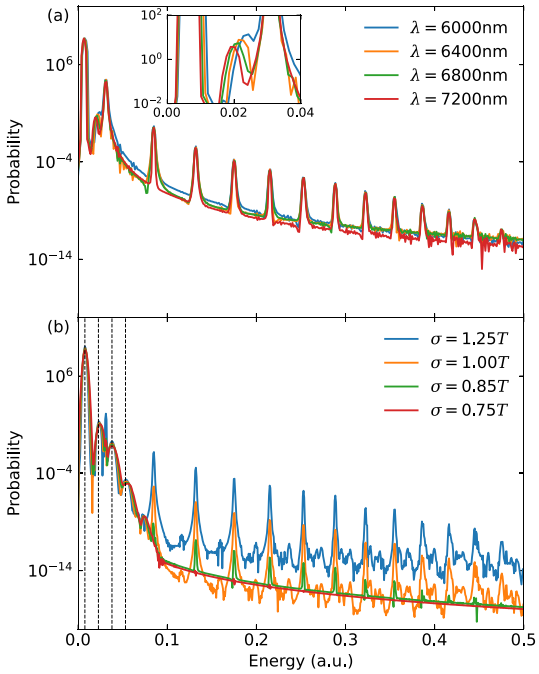

Figure 7. Dipole response spectra for the linear atomic chain with $N = 100$ and $a = 2$ a.u. under varying laser parameters: (a) wavelength dependence showing invariant plasmon peaks but shifting harmonic positions (see zoomin), and (b) pulse-width dependence using Gaussian-envelope pulses ($\lambda = 6000$ fixed), where T denotes the laser period. The dashed lines in panel (b) mark the first four odd harmonic orders ω, 3ω, 5ω, and 7ω.

escalates correspondingly. This leads to a reduction in the energy gaps between adjacent energy levels, which in turn results in a decrease in the plasmon resonance frequency, as evidenced in figure 5(a) [45]. Conversely, when the lattice constant a increases, the number of energy levels within the band stays constant. Yet, the energy gap between the highest and lowest energy levels in the band diminishes. This reduction causes an overall decrease in the energy gaps between adjacent energy levels, which also contributes to a lowering of the plasmon resonance frequency, as illustrated in figure 5(b). Hence, these two distinct modulation patterns are responsible for the observed frequency differences in plasmon resonance frequencies in figure 6, despite identical chain length.

The distinct origins of plasmon resonances and HHG lead to markedly different responses to laser field parameters. Plasmon frequencies, arising from collective electron excitations intrinsic to the atomic chain, remain unchanged with varying laser wavelength, as demonstrated in figure 7(a). This contrasts sharply with HHG signals, whose positions scale with the driving laser frequency, confirming their dependence on single-electron dynamics in the external field. Supporting this interpretation, carrier-free calculations, where the laser field has only an envelope but no carrier, show persistent plasmon peaks but completely absent HHG signals, further establishing plasmons as material properties rather than field-driven phenomena.

The influence of pulse duration reveals additional fundamental temporal distinctions between these excitation modes, as shown in figure 7(b). Using pulses with an Gaussian envelope $e^{-t^2/2\sigma^2}$ for better width control, we observe that plasmon resonance intensity depends strongly on pulse width. Specifically, a rapid attenuation of signal strength of plasmon resonance occurs when $\sigma < 0.75T$, with T the laser period. This pronounced pulse duration dependence reflects the fundamental timescale disparity between collective and individual excitations: plasmon resonance, as a many-body phenomenon, requires extended temporal intervals to establish coherent collective oscillations across the atomic chain, necessitating excitation durations spanning multiple laser cycles at current laser strength. Conversely, the HHG signal, marked by dashed lines, exhibits minor variation across σ ranges spanning $0.75T$ to $1.25T$, demonstrating its primary dependence on instantaneous field strength rather than interaction duration in current laser settings. This contrast highlights how HHG originates from sub-cycle single-electron dynamics, while plasmon formation involves cumulative many-body coherence developing over significantly longer timescales.

Notably, the modified Gaussian envelope reveals higher harmonic orders (figure 7(b)) while simultaneously permitting control over the relative intensity of plasmon versus HHG signals. These findings demonstrate that careful laser parameter selection, particularly pulse duration and envelope

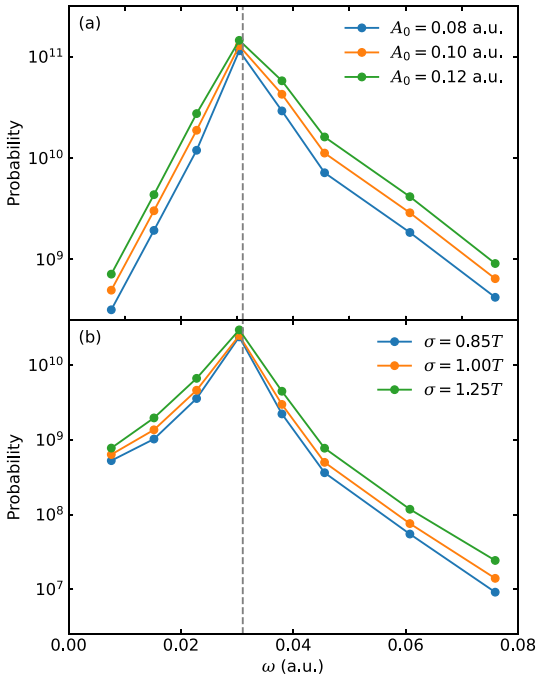

Figure 8. Maximum dipole response intensity of the linear atomic chain ($N = 100$, $a = 2$ a.u.) as a function of the laser frequency for (a) different vector potential amplitudes and (b) different pulse durations, where the same Gaussian envelope used in figure 7(b) is adopted for panel (b). The vertical dashed line indicates the fundamental plasmon resonance frequency ω_1 of the system.

shaping, provides powerful control over the competition between collective and single-particle excitations in nanoscale systems.

Plasmon-enhanced HHG was predicted in graphene systems [54] and subsequently detected in antenna-coupled silicon substrate [23], providing novel insights into the interaction between extreme nonlinear optics and plasmon. Our investigation of the resonant regime also reveals an enhancement profile when the laser frequency approaches the fundamental plasmon resonance ω_1 of the linear atomic chain with $N = 100$ and $a = 2$. As shown in figure 8, despite variations in laser parameters, the maximum dipole response intensity follows a pronounced resonance curve, exhibiting exponential growth as the laser frequency approaches ω_1 (marked by the dashed line), peaking at exact frequency matching, and subsequently decreasing exponentially in the off-resonant regime. This behavior confirms that maximum energy transfer occurs when the driving laser field is spectrally aligned with the system's intrinsic plasmon frequency.

Figure 8 further illustrates the dependence of the resonant enhancement on the laser field strength and pulse duration. As shown in figure 8(a), this enhancement becomes increasingly pronounced with decreasing vector potential amplitude, reflecting the strong sensitivity of harmonic signals to the laser field strength: as the field strength is reduced, the overall dipole response diminishes and the resonance-induced local field enhancement becomes more prominent. Therefore, in the weak-field limit, where the system response enters the linear regime and high-order harmonic signals are nearly absent, the presence of resonance can nevertheless enable harmonic emission through local field enhancement, resulting in a particularly strong contrast between resonant and off-resonant cases. Similarly, figure 8(b) shows that the resonant enhancement is also amplified for shorter pulse durations. As demonstrated in figure 7(b), reducing the pulse duration leads to only minor changes in the HHG signal intensity, while the plasmon resonance signal is significantly suppressed. Consequently, for short pulse durations, when the laser frequency approaches the fundamental plasmon resonance, the resulting resonant enhancement becomes more prominent. The associated local field generated under resonant condition therefore contributes more substantially to the overall signal enhancement than in the case of longer pulse durations. Overall, these results demonstrate that, in addition to intrinsic material properties, laser parameters provide an effective and flexible means to regulate the resonant response, thereby offering valuable insights and significant implications for the fundamental study of laser–matter interactions.

The dipole response displays additional complexity at higher frequencies, where the intensity reduction rate progressively diminishes when the laser frequency approaches 0.08. This attenuation suggests the onset of coupling to the second-order plasmon mode ω_2, revealing the system's multi-mode resonant

structure. Most notably, the resonant condition produces concurrent enhancement of both plasmon and harmonic signals, demonstrating non-trivial coupling between collective and single-particle excitation channels. This correlated amplification implies an energy transfer mechanism between these fundamentally different excitation modes during resonant driving conditions.

These observations establish that resonant excitation not only maximizes plasmon response but also enhances nonlinear optical processes in the system. This enhancement arises due to intense localized electric fields generated by laser-driven plasmon oscillations, which substantially amplify the optical nonlinearity [54]. The interdependence between plasmonic and harmonic generation signals points to a sophisticated relationship between collective and individual electron dynamics under strong driving fields, with important implications for controlling light-matter interactions in nanoscale systems.

5. Conclusion

In conclusion, through numerical modeling of a laser-driven linear atomic chain, we have systematically investigated and distinguished between two fundamental excitation modes in solid-state systems: collective plasmon resonances and single-particle HHG. Our results reveal three key insights:

First, plasmon resonances demonstrate a characteristic dependence on material parameters (atom number N and lattice constant a), while remaining insensitive to the driving laser frequency. However, their intensity can be effectively controlled through laser parameters, particularly via pulse width adjustment and frequency matching to the plasmon resonance condition.

Second, HHG shows complementary behavior that the harmonic frequencies are determined solely by the laser field, with intensities largely unaffected by pulse duration in current laser settings. This contrasting behavior provides a means to selectively enhance one excitation mode over the other through appropriate parameter tuning.

Third, we observe strong resonant enhancement at different laser parameters when the laser frequency approaches the plasmon resonance, leading to concurrent amplification of both plasmon and harmonic signals. This suggests non-trivial coupling between collective and single-particle excitations under resonant driving conditions.

These findings establish the linear atomic chain as a versatile platform for studying competing excitation mechanisms in condensed matter systems. The demonstrated control over relative mode intensities through parameter tuning opens new possibilities for investigating fundamental light-matter interactions in reduced-dimensionality systems. Furthermore, the observed resonant enhancement phenomena suggest promising directions for controlling nonlinear optical processes through plasmonic engineering.

Acknowledgements

We would like to thank Sheng Meng, Hongchuan Du and Shicheng Jiang for helpful discussions. This work was supported by the Quantum Science and Technology—National Science and Technology Major Project (Grant No. 2024ZD0300700), the National Natural Science Foundation of China (Grant Nos. 12474341, 12521003, 12227807, and 12241407), the Science and Technology Commission of Shanghai Municipality (Grant Nos. 23JC1402000 and 24YF2710000), and the Shanghai Pilot Program for Basic Research (Grant No. TQ20240204). Numerical computations were in part performed on the ECNU Multifunctional Platform for Innovation (001).

Data availability statement

The data that support the findings of this study are openly available at the following URL/DOI: https://doi.org/10.5281/zenodo.15 679 026 [55].

ORCID iDs

Hao Huang 0009-0000-9247-1544
Hongcheng Ni 0000-0003-4924-0921
Jian Wu 0000-0002-1318-2291

References

[1] Pines D 2018 Introductory survey *Elementary Excitations in Solids* ed D Pines pp 1–12
[2] Nie S and Emory S R 1997 Probing single molecules and single nanoparticles by surface-enhanced Raman scattering *Science* **275** 1102
[3] Xu H, Bjerneld E J, Kaöll M and Boörjesson L 1999 Spectroscopy of single hemoglobin molecules by surface enhanced Raman scattering *Phys. Rev. Lett.* **83** 4357
[4] Prodan E, Radloff C, Halas N J and Nordlander P 2003 A hybridization model for the plasmon response of complex nanostructures *Science* **302** 419
[5] Sönnichsen C, Franzl T, Wilk T, von Plessen G, Feldmann J, Wilson O and Mulvaney P 2002 Drastic reduction of plasmon damping in gold nanorods *Phys. Rev. Lett.* **88** 077402
[6] Li K, Stockman M I and Bergman D J 2003 Self-similar chain of metal nanospheres as an efficient nanolens *Phys. Rev. Lett.* **91** 227402
[7] Fang N, Lee H, Sun C and Zhang X 2005 Sub-diffraction-limited optical imaging with a silver superlens *Science* **308** 534
[8] Hervieux P-A and Bigot J-Y 2004 Surface plasmon dynamics of simple metal clusters excited with femtosecond optical pulses *Phys. Rev. Lett.* **92** 197402
[9] Jain P K, Huang X, El-Sayed I H and El-Sayed M A 2008 Noble metals on the nanoscale: optical and photothermal properties and some applications in imaging, sensing, biology and medicine *Acc. Chem. Res.* **41** 1578
[10] Karimi S, Moshaii A, Abbasian S and Nikkhah M 2019 Surface plasmon resonance in small gold nanoparticles: introducing a size-dependent plasma frequency for nanoparticles in quantum regime *Plasmonics* **14** 851
[11] Segovia P, Purdie D, Hengsberger M and Baer Y 1999 Observation of spin and charge collective modes in one-dimensional metallic chains *Nature* **402** 504
[12] Nagao T, Yaginuma S, Inaoka T and Sakurai T 2006 One-dimensional plasmon in an atomic-scale metal wire *Phys. Rev. Lett.* **97** 116802
[13] Qin H, Gao Y, Teng J, Xu H, Wu K and Gao S 2010 Laterally tunable plasmon resonance in confined biatomic-layer ag nanodisks *Nano Lett.* **10** 2961
[14] Ziman J M 1979 Electron states *Principles of the Theory of Solids* ed J M Ziman pp 77–118
[15] Ghimire S and Reis D A 2019 High-harmonic generation from solids *Nat. Phys.* **15** 10
[16] Heide C, Kobayashi Y, Haque S R U and Ghimire S 2024 Ultrafast high-harmonic spectroscopy of solids *Nat. Phys.* **20** 1546
[17] Wu M, Ghimire S, Reis D A, Schafer K J and Gaarde M B 2015 High-harmonic generation from bloch electrons in solids *Phys. Rev. A* **91** 043839
[18] Guan Z, Zhou X-X and Bian X-B 2016 High-order-harmonic generation from periodic potentials driven by few-cycle laser pulses *Phys. Rev. A* **93** 033852
[19] Ikemachi T, Shinohara Y, Sato T, Yumoto J, Kuwata-Gonokami M and Ishikawa K L 2017 Trajectory analysis of high-order-harmonic generation from periodic crystals *Phys. Rev. A* **95** 043416
[20] Ghimire S, DiChiara A D, Sistrunk E, Agostini P, DiMauro L F and Reis D A 2011 Observation of high-order harmonic generation in a bulk crystal *Nat. Phys.* **7** 138
[21] Vampa G, Hammond T, Thiré N, Schmidt B, Légaré F, McDonald C, Brabec T and Corkum P 2015 Linking high harmonics from gases and solids *Nature* **522** 462
[22] You Y S, Reis D A and Ghimire S 2017 Anisotropic high-harmonic generation in bulk crystals *Nat. Phys.* **13** 345
[23] Vampa G *et al* 2017 Plasmon-enhanced high-harmonic generation from silicon *Nat. Phys.* **13** 659
[24] Han S, Kim H, Kim Y W, Kim Y-J, Kim S, Park I-Y and Kim S-W 2016 High-harmonic generation by field enhanced femtosecond pulses in metal-sapphire nanostructure *Nat. Commun.* **7** 13105
[25] Bai Y, Fei F, Wang S, Li N, Li X, Song F, Li R, Xu Z and Liu P 2021 High-harmonic generation from topological surface states *Nat. Phys.* **17** 311
[26] Schmid C P *et al* 2021 Tunable non-integer high-harmonic generation in a topological insulator *Nature* **593** 385
[27] Li L, Lan P, Zhu X, Huang T, Zhang Q, Lein M and Lu P 2019 Reciprocal-space-trajectory perspective on high-harmonic generation in solids *Phys. Rev. Lett.* **122** 193901
[28] Jiang S, Chen J, Wei H, Yu C, Lu R and Lin C 2018 Role of the transition dipole amplitude and phase on the generation of odd and even high-order harmonics in crystals *Phys. Rev. Lett.* **120** 253201
[29] Yue L and Gaarde M B 2022 Introduction to theory of high-harmonic generation in solids: tutorial *J. Opt. Soc. Am. B* **39** 535
[30] Qian C, Yu C, Jiang S, Zhang T, Gao J, Shi S, Pi H, Weng H and Lu R 2022 Role of shift vector in high-harmonic generation from noncentrosymmetric topological insulators under strong laser fields *Phys. Rev. X* **12** 021030
[31] Vampa G, McDonald C, Orlando G, Klug D, Corkum P and Brabec T 2014 Theoretical analysis of high-harmonic generation in solids *Phys. Rev. Lett.* **113** 073901
[32] Hansen K K, Deffge T and Bauer D 2017 High-order harmonic generation in solid slabs beyond the single-active-electron approximation *Phys. Rev. A* **96** 053418
[33] Tancogne-Dejean N, Mücke O D, Kärtner F X and Rubio A 2017 Impact of the electronic band structure in high-harmonic generation spectra of solids *Phys. Rev. Lett.* **118** 087403
[34] Bauer D and Hansen K K 2018 High-harmonic generation in solids with and without topological edge states *Phys. Rev. Lett.* **120** 177401
[35] Drüeke H and Bauer D 2019 Robustness of topologically sensitive harmonic generation in laser-driven linear chains *Phys. Rev. A* **99** 053402
[36] Yu C, Jiang S and Lu R 2019 High order harmonic generation in solids: a review on recent numerical methods *Adv. Phys. X.* **4** 1562982
[37] Garg M, Kim H Y and Goulielmakis E 2018 Ultimate waveform reproducibility of extreme-ultraviolet pulses by high-harmonic generation in quartz *Nat. Photon.* **12** 291
[38] Park J, Subramani A, Kim S and Ciappina M F 2022 Recent trends in high-order harmonic generation in solids *Adv. Phys. X.* **7** 2003244
[39] Zhou H, Li D, Ren Z, Xu C, Wang L-F and Lee C 2024 Surface plasmons-phonons for mid-infrared hyperspectral imaging *Sci. Adv.* **10** eado3179
[40] Yazdanfar P, Heydarian H and Rashidian B 2020 Modal control of thermoplasmonic behavior of nanostructures based on excitation of perfect absorption resonances *J. Opt. Soc. Am. B* **37** 2238

[41] Zundel L, Malone K, Cerdan L, Martinez-Herrero R and Manjavacas A 2023 Lattice resonances for thermoplasmonics *ACS Photon.* **10** 274
[42] Liu J, Chen Y, Jin F, Wang J, Ikeda T and Jiang L 2022 Single-, dual-, triple and quadruple-wavelength surface-emitting lasing in blue-phase liquid crystal *Adv. Mater.* **34** 2108330
[43] Gao S and Yuan Z 2005 Emergence of collective plasmon excitation in a confined one-dimensional electron gas *Phys. Rev. B* **72** 121406
[44] Yan J, Yuan Z and Gao S 2007 End and central plasmon resonances in linear atomic chains *Phys. Rev. Lett.* **98** 216602
[45] Yan J and Gao S 2008 Plasmon resonances in linear atomic chains: free-electron behavior and anisotropic screening of d electrons *Phys. Rev. B* **78** 235413
[46] Yan L, Guan M and Meng S 2018 Plasmon-induced nonlinear response of silver atomic chains *Nanoscale* **10** 8600
[47] Pronin K A, Bandrauk A D and Ovchinnikov A A 1994 Harmonic generation by a one-dimensional conductor: Exact results *Phys. Rev. B* **50** 3473
[48] Li J, Zhang X, Fu S, Feng Y, Hu B and Du H 2019b Phase invariance of the semiconductor bloch equations *Phys. Rev. A* **100** 043404
[49] Yu C, Hansen K K and Madsen L B 2019b Enhanced high-order harmonic generation in donor-doped band-gap materials *Phys. Rev. A* **99** 013435
[50] Iravani H, Hansen K K and Madsen L B 2020 Effects of vacancies on high-order harmonic generation in a linear chain with band gap *Phys. Rev. Res.* **2** 013204
[51] Jensen S V B and Madsen L B 2021 Edge-state and bulk-like laser-induced correlation effects in high-harmonic generation from a linear chain *Phys. Rev. B* **104** 054309
[52] Bauer D and Fennel T 2017 How to propagate a wavefunction *Computational Strong-Field Quantum Dynamics: Intense Light-Matter Interactions* ed D Bauer pp 1–44
[53] Smith N V 1969 Optical constants of sodium and potassium from 0.5 to 4.0 eV by split-beam ellipsometry *Phys. Rev.* **183** 634
[54] Cox J D, Marini A and De Abajo F J G 2017 Plasmon-assisted high-harmonic generation in graphene *Nat. commun.* **8** 14380
[55] Huang H, Ni H and Wu J 2026 Collective and individual excitations in a linear atomic chain *Zenodo* (https://doi.org/10.5281/zenodo.15679026)